Rational Design of the β-Bulge Gate in a Green Fluorescent Protein Accelerates the Kinetics of Sulfate Sensing

Whitney S. Y. Ong[†§], Ke Ji[†§], Vishaka Pathiranage[‡§], Caden Maydew[†], Kiheon Baek[†], Rhiza Lyne E. Villones[†], Gabriele Meloni[†], Alice R. Walker[‡*], and Sheel C. Dodani[†*]

[†]Department of Chemistry and Biochemistry, The University of Texas at Dallas, Richardson, TX 75080

[‡]Department of Chemistry, Wayne State University, Detroit, MI 48202

[§]W.S.Y.O, K.J., and V.P contributed equally to this work.

*E-mail: sheel.dodani@utdallas.edu; arwalker@wayne.edu

Abstract:

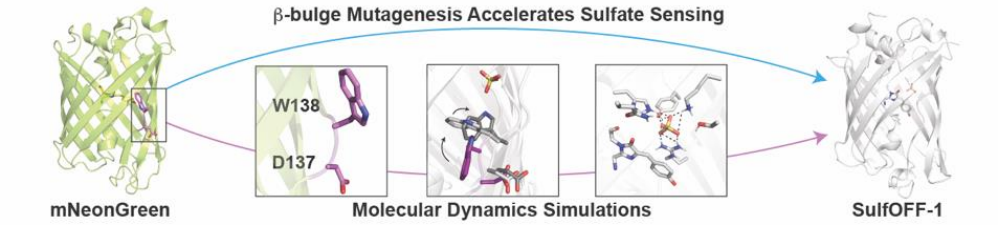

Detection of anions in complex aqueous media is a fundamental challenge with practical utility that can be addressed by supramolecular chemistry. Biomolecular hosts such as proteins can be used and adapted as an alternative to synthetic hosts. Here, we report how the mutagenesis of the β-bulge residues (D137 and W138) in mNeonGreen, a bright, monomeric fluorescent protein, unlocks and tunes the anion preference at physiological pH for sulfate, resulting in the turn-off sensor SulfOFF-1. This unprecedented sensing arises from an enhancement in the kinetics of binding, largely driven by position 138. In line with these data, molecular dynamics (MD) simulations capture how the coordinated entry and gating of sulfate into the β-barrel is eliminated upon mutagenesis to facilitate binding and fluorescence quenching.

Keywords: anions, molecular dynamics, protein engineering, sensor, supramolecular chemistry

Main Text

Halides and oxyanions are omnipresent in the environment and biology.[1–4] Synthetic hosts can be used to recognize, transport, and transform anionic guests in aqueous media for basic research and practical applications.[5–9] However, these remain underdeveloped for operation in pure water primarily due to the physical challenge of anion dehydration.[10–13] In this context, biomolecular hosts such as proteins typically inspire new synthetic designs but can in fact be used and adapted to achieve supramolecular functions.[5] On a molecular level, proteins are ideal because they combine cooperative, patterned interactions and the hydrophobic effect for aqueous anion detection.[14–18] Moreover, protein engineering can be used to rapidly diversify the encoding sequence space and enrich for hosts with desired properties (e.g., selectivity, affinity).[19–21] To decode these supramolecular principles, we are actively investigating, engineering, and applying protein-based hosts for anions.[22–28] Along these lines, we have a growing program focused on anion sensors derived from the green fluorescent protein (GFP) family.

GFP family members adopt a β-barrel structure and have a built-in chromophore derived from the cyclization and oxidation of a tripeptide that is typically based on tyrosine.[29,30] The chromophore can be sensitive to factors (e.g., pH, molecular oxygen, and ions) in the external and internal environments.[31–34] In 2019 we reported the identification and characterization of mNeonGreen (mNG) as a bright, monomeric, anion-sensitive fluorescent protein.[23,35] This discovery relied on a previously reported X-ray

crystal structure of mNG bound to chloride at pH 4.5.[36] The anion binding pocket consists of H62, R88, S153, T173 and Y175 and is near the tyrosine-based chromophore (Figure 1A).[27] The binding of halides and oxyanions shifts the chromophore equilibrium from the phenol to the phenolate state, generating a turn-on fluorescence response (Figure 1B).[23] Interestingly, the opposite is observed with sulfate.[23] However, these spectral changes only occur at acidic pH.[23] Nonetheless, in the context of anion-sensitive fluorescent proteins, mNG stands out because it recognizes an expanded set of anions and can access different sensing mechanisms.[23] To explore and develop the sensing potential of this platform, we are applying a structure-guided approach to identify positions for rational protein engineering .[27]

Along these lines, the gate post (A136/C139) and β-bulge (D137/W138) region is an attractive starting point because it is spatially near the chromophore and can readily be mutated to tune the photophysical features without significant perturbation to protein folding or chromophore maturation (Figure S1).[37] Closer inspection of this region in mNG reveals that the side chains of A136 and C139 are buried inward, whereas the main chains form hydrogen bonds with the β10 strand (avGFP notation) to stabilize the structure (Figure S1).[29,36] Interestingly, the sidechain of D137 is solvent exposed, while W138 adopts two different conformations, in and out of the β-barrel.[36] Based on these observations, the β-bulge could have a more pronounced impact on anion binding through electrostatic repulsion and/or steric gating. To test this hypothesis, here, we investigate the effect of glycine mutations at both positions by integrating photophysical measurements with molecular dynamics (MD) simulations.

To determine the outcome of our proposed rational design, we first expressed and purified mNG-D137G-W138G from *E. coli* and confirmed its monomeric oligomerization state (Figure S2–S3; Table S1). The absorbance and fluorescence response of mNG-D137G-W138G to halides and oxyanions of varying size, shape, and charge was screened at pH 7 (Figure 2A, 2B; Figure S4–S18). Consistent with the mNG parent, apo-mNG-D137G-W138G has an absorption maximum at 505 nm (ε = 94,511 ± 766 $M^{-1}{\cdot}cm^{-1}$) with a shoulder at 480 nm (Figure S19). These two absorption peaks arise from the phenolate chromophore.[23,36,38] Excitation of this state at 485 nm results in a single emission maximum at 520 nm (Φ = 0.69 ± 0.02) (Figure S20). No dramatic spectral changes are observed even in the presence of up to 100 mM chloride, bromide, iodide, nitrate, phosphate, and gluconate (Figure 2C; Figure S4–S18). However, the titration of sulfate triggers an immediate shift in the chromophore equilibrium from the phenolate (ε = 26,466 ± 831 $M^{-1}{\cdot}cm^{-1}$) to phenol state at 400 nm, resulting in fluorescence quenching (~69%, Φ = 0.59 ± 0.03) (Figure 2A, 2B; Table 1; Figure S19–S22). This fluorescence response data was fitted to a single site binding model to calculate the affinity (apparent dissociation constant, K_d) for sulfate to be 0.20 ± 0.01 (10^{-3}) M (Table 1; Figure S19–S20). Of the anions tested, sulfate has the most dramatic effect on the chromophore and stabilizes it in the phenol state as indicated by the shift in the pK_a from 5.65 ± 0.03 to 7.66 ± 0.09 (Table 1; Figure S23–S24). Given that mNG-D137G-W138G has a remarkable preference for sulfate, from here it will be referred to as SulfOFF-1 – the first intrinsic fluorescent protein-based sensor for sulfate at physiological pH.

With these results, we sought to understand the effect of each glycine mutation on sulfate sensing. For this, the mNG parent,-mNG-D137G, and mNG-W138G were prepared and characterized like SulfOFF-1 (Table 1; Figure S2–S3; Table S1; Figure S25–S87). However, unlike SulfOFF-1, all three proteins required overnight incubation for the spectra to equilibrate. The overall absorbance and emission profiles of each apo protein remain unchanged. To our surprise, the mNG parent and both mutants maintain a preference for sulfate with comparable degrees of fluorescence quenching (~69–74%). However, clear differences are observed in the sulfate binding affinities: mNG < mNG-W138G < mNG-D137G < SulfOFF-1. Interestingly, both single-point mutations lower the K_d and increase the affinity relative to the parent mNG, with a more pronounced effect at position 137. Because the latter is solvent exposed in the crystal structure, removal of the aspartate side chain could minimize electrostatic interactions (attractive or repulsive) with sulfate in the bulk solution. Closer inspection of the photophysical properties reveals subtle differences between the molar extinction coefficients, quantum yields, and pK_a values for all four proteins in the apo and sulfate-bound forms (Table 1). Notably, the extinction coefficient increases with the mutation at position 138. This points to the fact that the chromophore environment is perturbed and likely experiences a change in solvent accessibility.[39]

To further probe the observed time-dependence of sulfate binding, the kinetics of fluorescence quenching were measured for each protein under pseudo-first order conditions (Figure S88–S91).[40] All kinetic traces were fitted to a single exponential model to directly determine the on-rates of binding (k_{on}). These can be ranked as follows from slowest to fastest: mNG < mNG-D137G < mNG-W138G < SulfOFF-1 (Table 1; Figure S92). The off-rates of binding (k_{off}) were extrapolated using the K_d and k_{on} for each protein and are comparable in magnitude (10^{-3} s^{-1}). Considering the data on the extreme ends, sulfate binding to SulfOFF-1 is accelerated by 70-fold relative to the mNG parent. While both single-point mutations influence the k_{on}, position 138 plays a larger role likely due to the loss in steric hindrance imposed by the tryptophan side chain.

To dissect the individual and synergistic contributions of the β-bulge residues observed experimentally, we turned to a theoretical approach to build a molecular level picture.[41–43] Constant pH MD simulations at pH 7 were carried out for apo, apo with free diffusion of sulfates into mNG, and sulfate-bound forms of each protein (mNG, mNG-D137G, mNG-W138G, and SulfOFF-1) (Table S2).[44] For the diffusion simulations, free sulfate ions were added to the apo mNG system to capture the possible sulfate entry pathway. During the trajectories, sulfate ions are associated with three key regions on the surface of the protein composed of R103 (on the opposite side of the bulge region), R140 (close to the bulge region), and R172 (on the side of the beta barrel between them) (Figure 3). Of these, R140 is notably both near the β-beta bulge residues that are exposed to the bulk solvent and close to a nearby R195 residue located within the barrel, creating an outer and inner region of high positive charge. The passage of sulfate into the β-barrel is coordinated through a network of side chain interactions with W138 and R195 (Supporting Movie; Figure 4, apo and phase 1). Following this, R140 rotates into the protein and forms a new interaction, bringing sulfate closer to the chromophore (Figure 4, phases 2 and 3). The resulting coordination complex triggers a change in the chromophore orientation and restores the orientation of W138 (Figure 4, phase 3). This observation indicates that W138 undergoes a gating motion, providing an explanation for the relatively slower kinetics of sulfate binding to mNG.

Next, the trajectories for the apo and sulfate-bound forms of the proteins were analyzed. All systems showed equilibrated alpha carbon (C_α) root mean square deviations (RMSD) (less than 2.5 Å) after less than 10 ns of production, indicating overall stable structures (Figure S93). Upon examining the global protein conformations, no strong differences are found between the solvent-accessible surface areas (SASAs) (Figure S94–S95).[45]

There are subtle shifts (less than 500 $Å^2$) upon sulfate binding, particularly for the mNG-W138G and SulfOFF-1, which we associate with the loss of steric bulk from the mutation along with an overall tightening of hydrophobic residues in the active site (Table S3). However, the gap between the β7 and β10 strands (avGFP notation) widens as a function of the mutations.[29] Notably, the 137, 138, and 140 positions are on the β7 strand. To quantify the differences between each apo protein, the average distance (d) was measured between the alpha carbons of the residues at positions 140 and 198 (Figure 5; Figure S96). Comparatively, this opening is 2–5 Å wider in SulfOFF-1 (d > 18 Å). The root mean square fluctuation (RMSF) of residues 137–140 in mNG varies by less than 0.5 Å between apo and sulfate bound trajectories but shows a very large increase of up to 3 Å in apo SulfOFF-1, 1.5 Å in mNG-W138G, and a small increase of 1.0 Å in mNG-D137G (Figure S97). This is consistent with an overall increase of flexibility in this region. Together, these effects likely facilitate and accelerate the binding of sulfate.

By comparing the binding pocket in all four proteins, we observed that at any given time, there were always two charged residues (R88 and K143) and at least four polar residues within 4 Å to coordinate with the sulfate ion (Figure 6; Figure S98–S99; Table S4–S11). More notable differences are observed in the chromophore orientations upon sulfate binding within and between each system. The RMSF of the chromophore increases with sulfate and tracks with the experimentally measured binding affinity on the extreme ends: SulfOFF-1 > mNG (Figure S100). Given this, we speculate that the increased chromophore movement is correlated with a higher probability of fluorescence quenching via nonradiative decay. To fully explore this effect, additional computational work with electronic structure methods will be required and the subject of our future investigation.[46]

In summary, we have presented how the design of the β-bulge region in mNeonGreen serendipitously generates SulfOFF-1, a selective intrinsic fluorescent protein-based sensor for sulfate. The D137G and W138G mutations synergistically give rise to this function through a dramatic enhancement in the kinetics of binding. Furthermore, MD simulations provide a plausible explanation for these results by revealing how the β-bulge residues gate sulfate entry and coordination near the chromophore. To our knowledge, SulfOFF-1 is a unique example of a fluorescent sulfate sensor that holds promise for sulfate detection in complex aqueous applications ranging from environmental samples, biological fluids, and even living cells.[47–51] Together our data provides a rare glimpse of an intrinsic fluorescent protein sensor mechanism that could be generalized to other systems, warranting further exploration. Looking forward, we are excited by the possible outcomes from our collaborative approach to guide the design of protein-based hosts for anions to achieve supramolecular functions in aqueous environments.

Supporting Information

The experimental methods and supplemental data for this manuscript are provided in the supplementary material files.

Author Contributions

W.S.Y.O., K.J., and S.C.D. designed and carried out experiments and data analysis. C.M. and K.B. contributed to preliminary experiments. R.L.E.V. and G.M. contributed technical expertise for stopped-flow experiments and data analysis. V.P. and A.R.W. designed and performed computational modeling and analysis with assistance from K.J. W.S.Y.O., K.J., V.P., A.R.W., and S.C.D. wrote the manuscript with input from all co-authors.

Acknowledgements

Support for this study was provided by The University of Texas at Dallas (to S.C.D), the National Institute of General Medical Sciences of the National Institutes of Health (R35GM128704 to G.M., R35GM128923 to S.C.D), and the Welch Foundation (AT-1935-20170325 and AT-2073-20210327 to G.M., AT-1918-20170325 and AT-2060-20210327 to S.C.D). A.R.W. acknowledges the Wayne State supercomputing center for resources and support. This study does not represent the views of the funding sources.

Figures

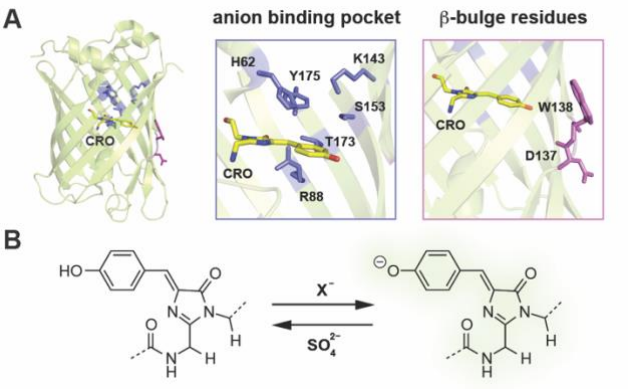

Figure 1. (A) X-ray crystal structure of mNeonGreen (mNG) with the chromophore (CRO) (PDB ID: 5LTP). The residues in the anion binding pocket and β-bulge are highlighted. Each residue is labeled with the single letter amino acid code and position number. (B) The chromophore equilibrium of mNG can be tuned between the non-fluorescent phenol and fluorescent phenolate states by anions at pH 4.5.

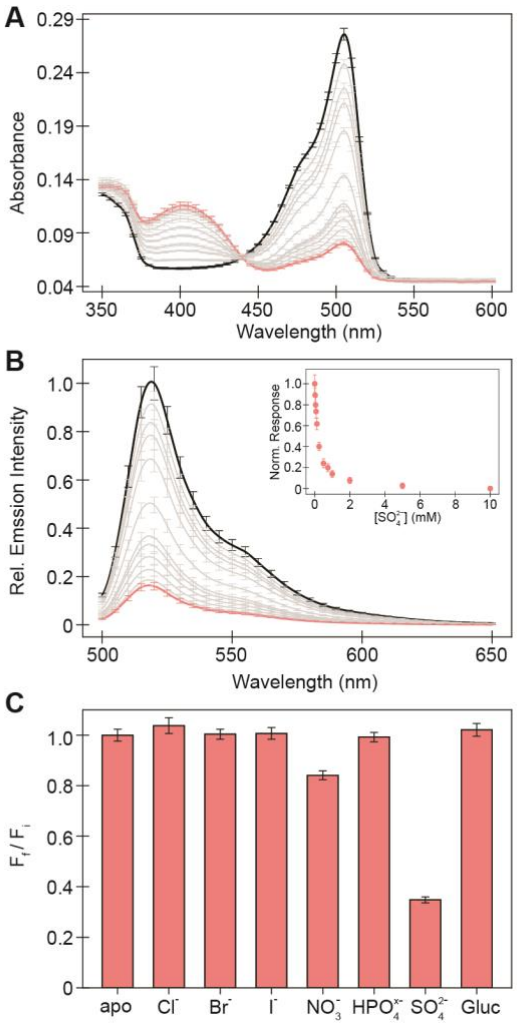

Figure 2. SulfOFF-1 (mNG-D137G-W138G) is a turn-off fluorescent sensor for sulfate. (A) Absorption and (B) emission spectra of SulfOFF-1 in the presence of 0 (black), 0.025, 0.05, 0.075, 0.125, 0.25, 0.5, 0.75, 1, 2, 5, and 10 mM (red) sulfate. The inset shows the normalized emission response at 520 nm as a function of increasing sulfate concentrations. (C) The fluorescence response (F_f / F_i) at 520 nm of SulfOFF-1 (apo, F_i) in the presence of 10 mM (F_f) sodium chloride (Cl^-), bromide (Br^-), iodide (I^-), nitrate (NO_3^-), phosphate ($H_2PO_4^-$/HPO_4^{2-}), sulfate (SO_4^{2-}), and gluconate (Gluc). Data was collected in triplicate from two protein preparations and is reported as the average with standard error of the mean. All experiments were carried out at room temperature (23–25 °C) with 4 μM protein in 50 mM MOPS and 1 mM NaCl buffer at pH 7 (λ_{ex} = 485 nm, λ_{em} = 500–650 nm).

Table 1. Summary of thermodynamic, kinetic, and photophysical parameters derived from steady state and time-resolved spectroscopic measurements for mNG, mNG-D137G, mNG-W138G, and SulfOFF-1 with sulfate. Data was collected in triplicate from two protein preparations and is reported as the average with standard error of the mean. All experiments were carried out at room temperature (23–25 °C) with 4 µM protein in 50 mM MOPS and 1 mM NaCl buffer at pH 7.

		mNG	mNG-D137G	mNG-W138G	SulfOFF-1
K_d (× 10^{-3} M)		1.37 ± 0.22	0.34 ± 0.03	0.57 ± 0.04	0.20 ± 0.01
k_{on} ($M^{-1}·s^{-1}$)		0.02 ± 0.01	0.06 ± 0.01	0.14 ± 0.01	1.06 ± 0.04
k_{off} (×10^{-3} s^{-1})		0.02 ± 0.01	0.02 ± 0.00	0.08 ± 0.01	0.22 ± 0.01
pK_a	apo	5.30 ± 0.04	5.61 ± 0.11	5.52 ± 0.01	5.65 ± 0.03
	+ SO_4^{2-}	7.15 ± 0.07	7.61 ± 0.05	7.32 ± 0.04	7.66 ± 0.09
Molar Extinction Coefficient ($M^{-1}·cm^{-1}$)	apo	87,773 ± 340	84,442 ± 669	96,810 ± 285	94,511 ± 766
	+ SO_4^{2-}	33,264 ± 277	21,637 ± 318	28,800 ± 295	26,466 ± 831
Quantum Yield	apo	0.77 ± 0.00	0.70 ± 0.01	0.73 ± 0.01	0.69 ± 0.02
	+ SO_4^{2-}	0.69 ± 0.00	0.57 ± 0.01	0.71 ± 0.01	0.59 ± 0.03
Molar Brightness	apo	67.59 ± 0.37	59.11 ± 0.97	70.67 ± 0.99	65.21 ± 1.96
	+ SO_4^{2-}	22.95 ± 0.20	12.33 ± 0.28	20.45 ± 0.36	15.61 ± 0.93

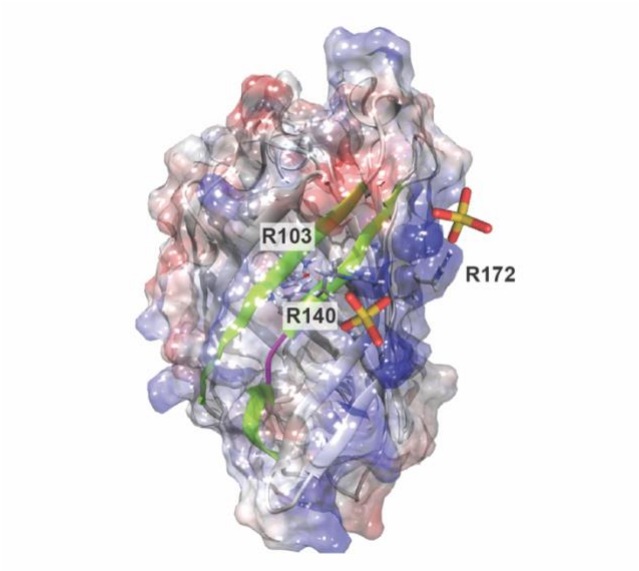

Figure 3. Surface potential map of mNG generated by molecular dynamics (MD) simulations where a high density of positive charge is in blue and negative charge is in red. Sulfate binding hotspots are associated with the solvent-exposed residues R103, R140 and R172 in the region of positive charge density. The key R residues near the β-bulge and the surface-bound sulfate ions prior to entry are shown.

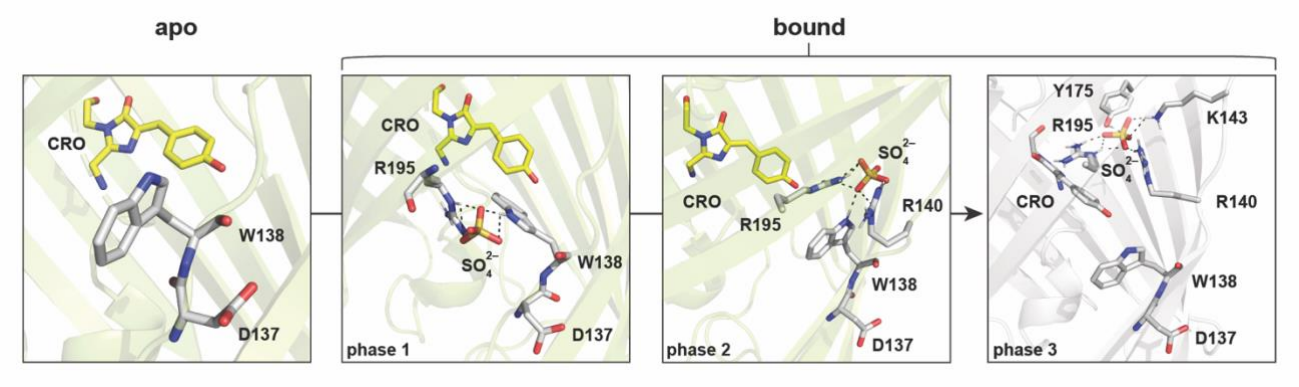

Figure 4. MD simulations reveal a pathway for sulfate entry and binding in mNG at the β-bulge gate. Representative snapshots are shown for the apo and sulfate-bound phases with possible hydrogen bonding and electrostatic interactions within 4 Å (dashed lines).

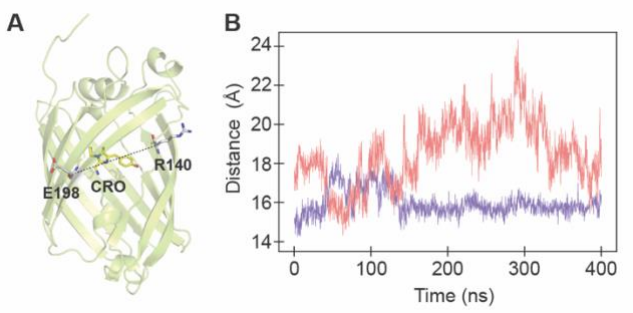

Figure 5. MD simulations indicate that SulfOFF-1 has the widest opening to facilitate the binding of sulfate. (A) Representative snapshot of SulfOFF-1 to highlight the opening that is defined as the distance (dashed line) between the Cα atoms of residues R140 and E198. (B) Analysis of the distances for mNG (purple) and SulfOFF-1 (red) as a function of time for a representative trajectory.

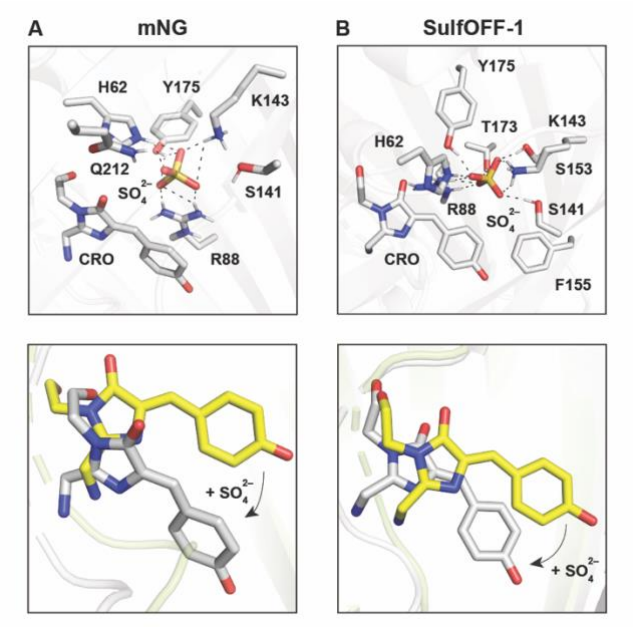

Figure 6. MD simulations show how sulfate binding induces a change in the chromophore orientation leading to fluorescence quenching in (A) mNG and (B) SulfOFF-1. A snapshot from each sulfate-bound trajectory is shown in the top panel. Possible hydrogen bonding or electrostatic interactions within 4 Å of sulfate are shown with dashed lines. Comparison of the chromophores in the apo (white) and sulfate-bound (yellow) trajectories for each protein is shown in the bottom panel. All snapshots are taken from the last frame of a representative trajectory.

References

[1] Y.-Y. Wang, Y.-H. Cheng, K.-E. Chen, Y.-F. Tsay, *Annu. Rev. Plant Biol.* **2018**, *69*, 85–122.
[2] Y. B. Yin, S. Guo, K. N. Heck, C. A. Clark, C. L. Conrad, M. S. Wong, *ACS Sustain. Chem. Eng.* **2018**, *6*, 11160–11175.
[3] M. Zajac, K. Chakraborty, S. Saha, V. Mahadevan, D. T. Infield, A. Accardi, Z. Qiu, Y. Krishnan, *J. Cell Sci.* **2020**, *133*, jcs240390.
[4] M. Q. Bowlin, M. J. Gray, *Trends Microbiol.* **2021**, *29*, 1013–1023.
[5] N. Busschaert, C. Caltagirone, W. Van Rossom, P. A. Gale, *Chem. Rev.* **2015**, *115*, 8038–8155.
[6] S. A. Boer, E. M. Foyle, C. M. Thomas, N. G. White, *Chem. Soc. Rev.* **2019**, *48*, 2596–2614.
[7] W. Han, W. Xiang, Q. Li, H. Zhang, Y. Yang, J. Shi, Y. Ji, S. Wang, X. Ji, N. M. Khashab, J. L. Sessler, *Chem. Soc. Rev.* **2021**, *50*, 10025–10043.
[8] L. K. Macreadie, A. M. Gilchrist, D. A. McNaughton, W. G. Ryder, M. Fares, P. A. Gale, *Chem* **2022**, *8*, 46–118.
[9] E. A. Kataev, *Chem. Commun.* **2023**, *59*, 1717–1727.
[10] M. J. Langton, C. J. Serpell, P. D. Beer, *Angew. Chemie Int. Ed.* **2016**, *55*, 1974–1987.
[11] L. Qin, S. J. N. Vervuurt, R. B. P. Elmes, S. N. Berry, N. Proschogo, K. A. Jolliffe, *Chem. Sci.* **2020**, *11*, 201–207.
[12] X. Wu, A. M. Gilchrist, P. A. Gale, *Chem* **2020**, *6*, 1296–1309.
[13] N. Tzioumis, D. Cullen, K. Jolliffe, N. G. White, *Angew. Chemie Int. Ed.* **2023**, e202218360.
[14] S. Mangani, M. Ferraroni, in *Supramol. Chem. Anions* (Eds.: A. Bianchi, K. Bowman-James, E. García-España), Wiley-VCH, New York, USA, **1997**, pp. 63–78.
[15] S. Kubik, *Chem. Soc. Rev.* **2009**, *38*, 585–605.
[16] H. I. Okur, J. Hladílková, K. B. Rembert, Y. Cho, J. Heyda, J. Dzubiella, P. S. Cremer, P. Jungwirth, *J. Phys. Chem. B* **2017**, *121*, 1997–2014.
[17] W. Yao, K. Wang, A. Wu, W. F. Reed, B. C. Gibb, *Chem. Sci.* **2021**, *12*, 320–330.
[18] J. W. Steed, J. L. Atwood, in *Supramol. Chem.*, Wiley, Chichester, UK, **2022**, pp. 265–350.
[19] W. H. J. Ward, D. Timms, A. R. Fersht, *Trends Pharmacol. Sci.* **1990**, *11*, 280–284.
[20] M. S. Packer, D. R. Liu, *Nat. Rev. Genet.* **2015**, *16*, 379–394.
[21] E. C. Alley, G. Khimulya, S. Biswas, M. AlQuraishi, G. M. Church, *Nat. Methods* **2019**, *16*, 1315–1322.
[22] J. N. Tutol, W. Peng, S. C. Dodani, *Biochemistry* **2019**, *58*, 31–35.
[23] J. N. Tutol, H. C. Kam, S. C. Dodani, *ChemBioChem* **2019**, *20*, 1759–1765.
[24] J. N. Tutol, J. Lee, H. Chi, F. N. Faizuddin, S. S. Abeyrathna, Q. Zhou, F. Morcos, G. Meloni, S. C. Dodani, *Chem. Sci.* **2021**, *12*, 5655–5663.
[25] K. Ji, K. Baek, W. Peng, K. A. Alberto, H. Torabifard, S. O. Nielsen, S. C. Dodani, *Chem. Commun.* **2022**, *58*, 965–968.
[26] H. Chi, Q. Zhou, J. N. Tutol, S. M. Phelps, J. Lee, P. Kapadia, F. Morcos, S. C. Dodani, *ACS Synth. Biol.* **2022**, *11*, 1627–1638.
[27] J. N. Tutol, W. S. Y. Ong, S. M. Phelps, W. Peng, H. Goenawan, S. C. Dodani, *bioRxiv preprint* **2022**, DOI: 10.1101/2022.08.13.503807.
[28] W. Peng, C. C. Maydew, H. Kam, J. K. Lynd, J. N. Tutol, S. M. Phelps, S. Abeyrathna, G. Meloni, S. C. Dodani, *Chem. Sci.* **2022**, *13*, 12659–12672.
[29] R. Y. Tsien, *Annu. Rev. Biochem.* **1998**, *67*, 509–544.
[30] Y. A. Labas, N. G. Gurskaya, Y. G. Yanushevich, A. F. Fradkov, K. A. Lukyanov, S. A. Lukyanov, M. V. Matz, *Proc. Natl. Acad. Sci.* **2002**, *99*, 4256–4261.
[31] S. Jayaraman, P. Haggie, R. M. Wachter, S. J. Remington, A. S. Verkman, *J. Biol. Chem.* **2000**, *275*, 6047–6050.
[32] H. Tsutsui, S. Karasawa, Y. Okamura, A. Miyawaki, *Nat. Methods* **2008**, *5*, 683–685.
[33] M. Tantama, Y. P. Hung, G. Yellen, *J. Am. Chem. Soc.* **2011**, *133*, 10034–10037.
[34] M. Schwarzländer, T. P. Dick, A. J. Meyer, B. Morgan, *Antioxid. Redox Signal.* **2016**, *24*, 680–712.
[35] N. C. Shaner, G. G. Lambert, A. Chammas, Y. Ni, P. J. Cranfill, M. A. Baird, B. R. Sell, J. R. Allen, R. N. Day, M. Israelsson, M. W. Davidson, J. Wang, *Nat. Methods* **2013**, *10*, 407–409.
[36] D. Clavel, G. Gotthard, D. von Stetten, D. De Sanctis, H. Pasquier, G. G. Lambert, N. C. Shaner, A. Royant, *Acta Crystallogr. Sect. D Struct. Biol.* **2016**, *72*, 1298–1307.
[37] Y. Nasu, Y. Shen, L. Kramer, R. E. Campbell, *Nat. Chem. Biol.* **2021**, *17*, 509–518.
[38] F. Steiert, E. P. Petrov, P. Schultz, P. Schwille, T. Weidemann, *Biophys. J.* **2018**, *114*, 2419–2431.
[39] R. M. Wachter, M.-A. Elsliger, K. Kallio, G. T. Hanson, S. J. Remington, *Structure* **1998**, *6*,

1267–1277.
[40] X. Zheng, C. Bi, Z. Li, M. Podariu, D. S. Hage, *J. Pharm. Biomed. Anal.* **2015**, *113*, 163–180.
[41] E. Y. Lau, J. L. Phillips, M. E. Colvin, *Mol. Phys.* **2009**, *107*, 1233–1241.
[42] S. Mukherjee, S.-T. Hung, N. Douglas, P. Manna, C. Thomas, A. Ekrem, A. E. Palmer, R. Jimenez, *Biochemistry* **2020**, *59*, 3669–3682.
[43] S. Mukherjee, R. Jimenez, *J. Phys. Chem. B* **2022**, *126*, 735–750.
[44] D. A. Case, I. Y. Ben-Shalom, S. R. Brozell, D. S. Cerutti, I. T.E. Cheatham, V. W. D. Cruzeiro, T. A. Darden, R. E. Duke, D. Ghoreishi, M. K. Gilson, H. Gohlke, A. W. Goetz, D. Greene, R. Harris, N. Homeyer, Y. Huang, S. Izadi, A. Kovalenko, T. Kurtzman, T. S. Lee, S. LeGrand, P. Li, C. Lin, J. Liu, T. Luchko, R. Luo, D. J. Mermelstein, K. M. Merz, Y. Miao, G. Monard, C. Nguyen, H. Nguyen, I. Omelyan, A. Onufriev, F. Pan, R. Qi, D. R. Roe, A. Roitberg, C. Sagui, S. Schott-Verdugo, J. Shen, C. L. Simmerling, J. Smith, R. Salomon-Ferrer, J. Swails, R. C. Walker, J. Wang, H. Wei, R. M. Wolf, X. Wu, L. Xiao, D. M. York, P. A. Kollman, **2018**.
[45] W. Humphrey, A. Dalke, K. Schulten, *J. Mol. Graph.* **1996**, *14*, 33–38.
[46] C. M. Jones, N. H. List, T. J. Martínez, *J. Am. Chem. Soc.* **2022**, *144*, 12732–12746.
[47] J. A. Schiff, R. C. Hodson, *Annu. Rev. Plant Physiol.* **1973**, *24*, 381–414.
[48] D. E. . Cole, J. Evrovski, *J. Chromatogr. A* **1997**, *789*, 221–232.
[49] R. Langford, E. Hurrion, P. A. Dawson, *J. Genet. Genomics* **2017**, *44*, 7–20.
[50] U. Fatima, M. K. Okla, M. Mohsin, R. Naz, W. Soufan, A. A. Al-Ghamdi, A. Ahmad, *Int. J. Mol. Sci.* **2020**, *21*, 2572.
[51] D. Zak, M. Hupfer, A. Cabezas, G. Jurasinski, J. Audet, A. Kleeberg, R. McInnes, S. M. Kristiansen, R. J. Petersen, H. Liu, T. Goldhammer, *Earth-Science Rev.* **2021**, *212*, 103446.